Reprinted from
PHILOSOPHICAL MAGAZINE, Vol. 12, No. 115, p. 177, July 1965

An X-ray Topographic Study of Planar Growth Defects in a Natural Diamond

By B. LAWN, Y. KAMIYA and A. R. LANG
H. H. Wills Physics Laboratory, University of Bristol

[Received 15 January 1965, and in revised form 11 February 1965]

ABSTRACT

Ten outcropping planar defects 30 to 70 μm in edge length lying in {111} planes inclined to the octahedral faces of an unusually perfect diamond (diameter 4 mm) were revealed by diffraction contrast but could not be detected optically. Those defects in the form of an equilateral triangle with one edge in the crystal surface show stacking-fault-type fringes and are bounded by Frank sessile dislocations. A single regular tetrahedral fault surface lying wholly within the crystal produces a type of X-ray interference not previously observed. Its diffraction theory is outlined, and computed fringe positions and spacings agree well with observation.

§ 1. INTRODUCTION

IMPERFECTIONS within diamonds may be studied by X-ray topography without destruction of the specimen. The techniques employed and some of their findings have been reviewed by Frank and Lang (1965). Recently, as part of a study of the abrasion of diamond (Lawn, Lang and E. Wilks, in preparation) we have made a topographic study of an unusually perfect stone, and have discovered therein local planar defects of a type not seen previously in the course of surveys of some dozens of specimens. The defects lie in well-defined crystallographic orientations. All are parallel to {111}. With one exception they outcrop at natural octahedral faces. One defect, in form a regular tetrahedron with faces parallel to {111}, was contained wholly within the crystal.

Poles of planes used for topograph reflections are indexed in the stereographic projection on $(00\bar{1})$, fig. 1. A sketch of the stone, oriented similarly to the projection, is placed at the figure centre. Originally the stone was a somewhat irregular octahedron. When examined by us it had a pair of opposite apices truncated and polished to form large $(00\bar{1})$ and small (001) facets respectively, and one edge was polished away to produce a $(\bar{1}\bar{1}0)$ facet.

On the $2\bar{2}0$, $\bar{2}20$ stereopair of projection topographs (figs. 2 (*a*) and (*b*)) the following features may be noted. Flecks of blackening on images of natural faces reveal the abundance of scratches and ring-cracks. Burrs on edges produce lines of blackening which are helpful in indicating the outline of the stone. Corners are badly chipped and bruised and give especially intense reflections. Within the stone the density of dislocations

Fig. 1

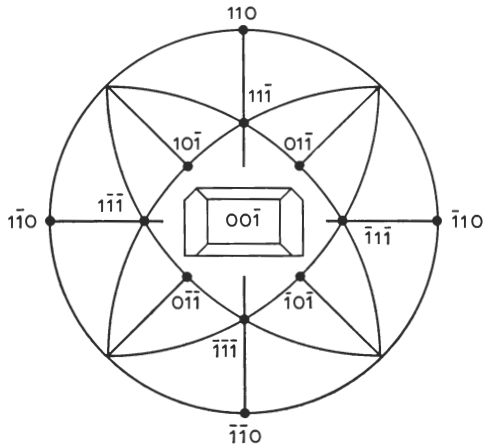

Stereographic projection on (00$\bar{1}$). Sketch of stone at centre.

is exceptionally low. The majority of those present radiate from a central imperfection. Images of the polished facets show no surface damage. Instead they display a series of concentric 'picture-frames' of enhanced diffracting power. These arise from local lattice curvature where the artificially cut facets intersect natural {111} growth stratifications and allow relaxation of grown-in stresses due presumably to varying impurity content. Such stratifications record the history of growth of the crystal since they show successive positions of the surface of the growing crystal, i.e. of growth horizons.

The features described above are all familiar in x-ray topography of diamond (Frank and Lang 1959, 1965, Lang 1964.) Man-made features

Fig. 2

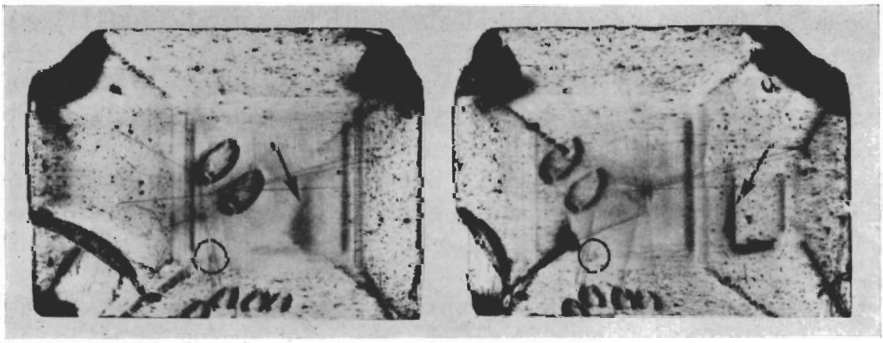

(*a*) (*b*)

Stereopair of projection topographs, Mo Kα radiation. Crystal width is 4 mm. Interior tetrahedron circled, imperfect layer parallel to ($\bar{1}$11) arrowed. (*a*) 2$\bar{2}$0 reflection, (*b*) $\bar{2}$20 reflection.

peculiar to the topographs here shown are the ellipses of blackening arising from cuts made with the edge of a rotating double conical wheel used in the abrasion tests (Wilks and Wilks 1959, Wilks 1961). We see two cuts parallel to [010] on [00$\bar{1}$], and four parallel to [11$\bar{2}$] on [$\bar{1}\bar{1}\bar{1}$]. An unusual natural feature is the diffuse triangular sheet of enhanced diffracting power parallel to a ($\bar{1}$11) plane within the crystal (arrowed in figs. 2 (*a*) and (*b*)). This sheet will be discussed in § 4. The outcropping defects of present interest are all less than 70 μm in maximum dimension and are not readily seen at the low magnifications of fig. 2. They appear as small dark triangles. The majority outcrop on the (11$\bar{1}$) face. Single examples have been detected in ($\bar{1}$1$\bar{1}$) and ($\bar{1}\bar{1}$1). The interior tetrahedral defect, seen faintly within the circles on figs. 2 (*a*) and (*b*), lies a little more than half-way from the cube plane containing the central imperfection to the (00$\bar{1}$) facet.

In addition to the x-ray diffraction studies we have examined the stone by transmitted polarized light, by scattered light, and by x-ray absorption topography. Phase contrast micrographs have been taken of the (11$\bar{1}$) surface. None of the planar defects here discussed were revealed in these additional examinations.

For convenience we will discuss the outcropping defects and the interior tetrahedral defect separately, in § 2 and § 3 respectively. In § 4 we will draw some general conclusions concerning the growth history of the diamond.

§ 2. Outcropping Defects

For various reasons (chief of which is the reduction of extinction distance with increasing wavelength) better resolution is achieved with Cu Kα than with Mo Kα radiation. A set of topographs of the (11$\bar{1}$) face was taken with Cu Kα radiation, using the 1$\bar{1}\bar{1}$, 111, $\bar{1}$1$\bar{1}$, 20$\bar{2}$, 220 and 02$\bar{2}$ reflections. In all cases it could be arranged that the diffracted beam left the (11$\bar{1}$) face nearly normally so as to form an undistorted topographic image. When necessary, the technique of 'limited projection topographs' (Lang 1963) was used to eliminate the unwanted images from other parts of the crystal. In fig. 3 are shown the 1$\bar{1}\bar{1}$, 111 and $\bar{1}$1$\bar{1}$ topographs of the corner of the (11$\bar{1}$) face close to the (1$\bar{1}\bar{1}$) face and (00$\bar{1}$) facet. This corner has the highest density of outcropping defects. Different variations across the topographs of image density and contrast arise from unavoidable differences in absorbing path through the crystal taken by the rays in each case. The corner of the (00$\bar{1}$) facet included in the field shows the growth stratifications clearly.

The outcropping planar defects appear to occupy equilateral triangles on one or more of the {111} planes intersecting (11$\bar{1}$). One edge of each triangle lies in the (11$\bar{1}$) surface. This configuration leads us to expect the three basic forms sketched in fig. 4, viz. triangles on a single plane, dihedra and trihedra. We do observe single-plane defects (e.g. those in

fig. 3 marked A, parallel to $(\bar{1}1\bar{1})$, and B, parallel to $(1\bar{1}\bar{1})$), and also trihedra (marked T in fig. 3); but we have not found dihedra on any face.

The defects exhibit no *area* diffraction contrast when their plane coincides with the Bragg plane, nor in 220-type reflections from planes in the zone normal to the defect plane. Other 111 and 220-type reflections show area contrast which under favourable geometrical conditions is resolved into

Fig. 3

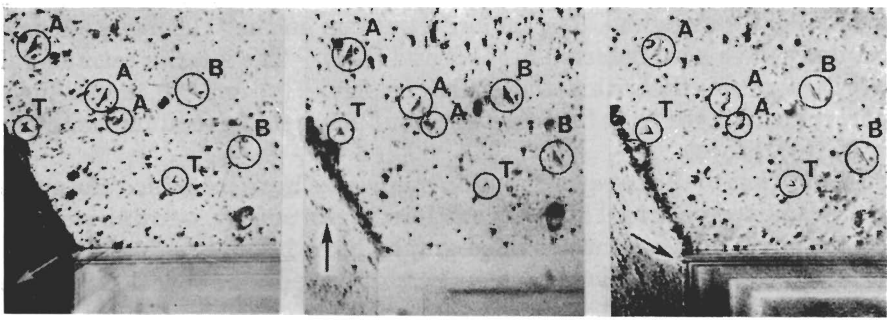

(*a*) (*b*) (*c*)

Topographs of part of $(11\bar{1})$ face, with part of $(00\bar{1})$ facet included in lower right of field. Cu Kα radiation. Arrows, length 150 μm, are projections of diffraction vector. Circles A indicate triangles parallel to $(\bar{1}1\bar{1})$; B, triangles parallel to $(1\bar{1}\bar{1})$; and T, trihedra. (*a*) $1\bar{1}\bar{1}$ reflection, (*b*) 111 reflection, (*c*) $\bar{1}1\bar{1}$ reflection.

stacking-fault-type fringes with the familiar Pendellösung depth periodicity of about 20 μm. Thus in each of the 111-type reflections the two sides of a trihedron which are not parallel with the Bragg plane produce contrast, as shown in the enlargements in figs. 5 (*a*), (*b*) and (*c*). The trihedra appearing in fig. 3 are too small to show more than the first Pendellösung maximum. The larger single-plane defects (A, B) have their apices (N, fig. 4) about 55 μm below the surface and show three fringes (fig. 5 (*d*)).

It is beyond the resolving power of the x-ray topographs to detect any line contrast from edges of a trihedron in the presence of area contrast

Fig. 4

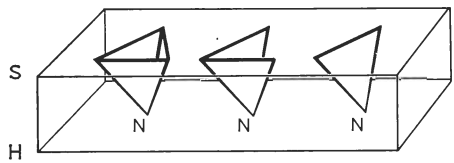

Expected basic forms of grown-in plane defects initiated at nuclei N on horizon H and propagated outwards to crystal surface S; trihedron, dihedron, and triangle.

from its faces, but we do observe dislocation-line contrast from the edges of the single-plane defects in those reflections which give no area contrast. Figure 5 (*e*) is an enlargement of a defect in orientation A, i.e. parallel to $(\bar{1}1\bar{1})$, taken with the $\bar{1}1\bar{1}$ reflection. That this curious pattern does arise from a pair of dislocations diverging from the apex and running out to the surface along [110] and $[10\bar{1}]$ respectively may be understood from the following observations. Firstly, consider the two isolated dislocations which outcrop in the field of fig. 3. They appear on fig. 3 (*a*) only: one is on the left of the upper defect B and the other below and to the left of the lower defect B. Both dislocations have Burgers vector parallel to $[10\bar{1}]$ and are mainly screw. They give sharp images near their points of outcrop, but the images from segments below the surface get rapidly wider and weaker with increasing segment depth. This widening arises from the fanning-out of the diffraction effects of the dislocation within the whole 'energy-flow triangle' contained between incident and diffracted beam directions. The angle $2\theta_B$ included between these directions, 44°, is large in the present case. Near the outcrop the sharp dislocation

Fig. 5

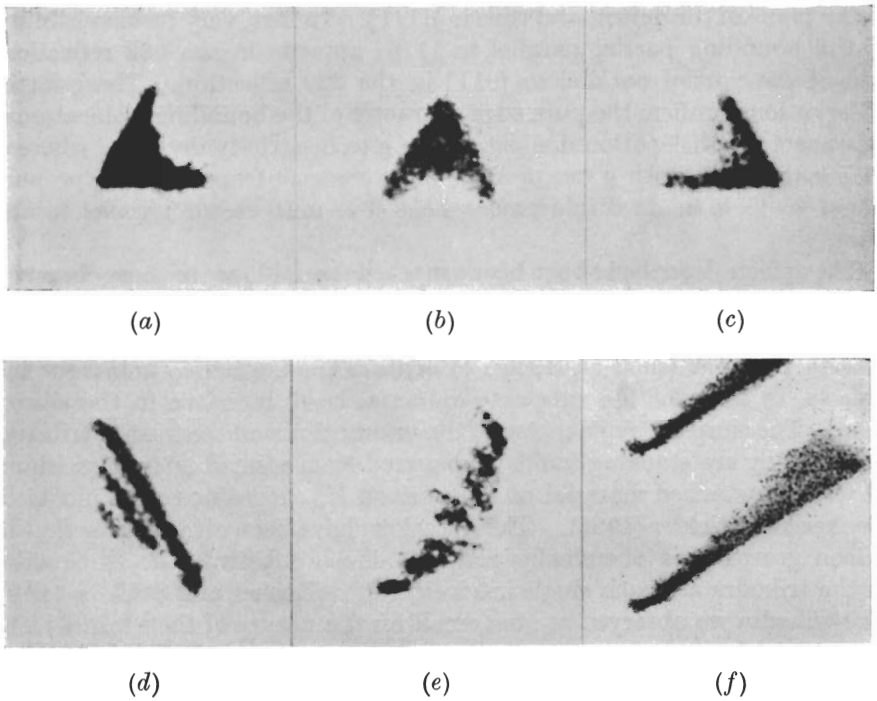

Enlargements of images of outcropping defects shown in fig. 3. (Images of surface damage have been subdued.) Trihedron in reflections (*a*) $1\bar{1}\bar{1}$, (*b*) 111, (*c*) $\bar{1}1\bar{1}$, (*d*) triangle parallel to $(1\bar{1}\bar{1})$, reflection $\bar{1}1\bar{1}$, (*e*) triangle parallel to $(\bar{1}1\bar{1})$, reflection $\bar{1}1\bar{1}$, (*f*) outcropping dislocations in silicon, for comparison with image (*e*).

image has the familiar Pendellösung beading; further away this changes to a 'feathering' or 'barbing' of the image. It is these barbs which we see chiefly in fig. 5(*e*). The two images shown for comparison in fig. 5(*f*) are of dislocations in silicon taken with Mo Kα radiation. For them the energy flow-triangle is much narrower and their barbs are not so pronounced. They are, however, viewed in an orientation similar to the lower bounding dislocation (parallel to $[10\bar{1}]$) in fig. 5(*e*). If a mirror be placed on one of the fig. 5(*f*) images in the position corresponding to the mirror plane of the image of fig. 5 (*e*) then the latter pattern can be convincingly synthesized.

We find that the dislocations bounding all single-plane defects are Frank sessiles. We will review the evidence for this conclusion with respect to defects in the orientation B. Figure 3(*a*) shows that the contrast of the bounding dislocations is closely similar to that of the two isolated dislocations having Burgers vector $\frac{1}{2}[10\bar{1}]$. For the latter, in this $1\bar{1}\bar{1}$ reflection, $\mathbf{g}.\mathbf{b}=1$. Since x-ray topographic dislocation image contrast depends quite strongly upon the value of $\mathbf{g}.\mathbf{b}$ under the experimental conditions applying, we conclude that $\mathbf{g}.\mathbf{b}=1$ also for the bounding dislocations. Since, to a first order, the bounding dislocations are invisible in the 220 and $02\bar{2}$ reflections, we conclude that $\mathbf{b}$ is normal to the plane of the defect, and thus is $\frac{1}{3}[1\bar{1}1]$. In fact, very feeble visibility of the bounding partial parallel to [110] appears in the $02\bar{2}$ reflection, and of the partial parallel to $[01\bar{1}]$ in the 220 reflection. These latter observations confirm the pure edge character of the bounding dislocations: we expect the dislocation line parallel to $\mathbf{g}$ to be strictly invisible, whereas that making 60° with $\mathbf{g}$ can produce faint contrast from the term proportional to $\mathbf{l}\times\mathbf{b}$ in its displacement field ($\mathbf{l}$ is unit vector parallel to the line).

The defects described above bear a marked resemblance to those observed in electron microscopy of epitaxially grown layers of silicon on silicon (Booker and Stickler 1962, Booker 1965). In the present examples certain growth horizons (such as H, fig. 4) contain the nucleating points for the defects, in place of the substrate-epitaxial layer interface in the silicon case. The simplest explanation of the orientation and contrast of trihedra is that they are stacking faults propagated from a small triangular island of wrongly stacked material at the horizon H, according to the model of Booker and Stickler (1962). These workers have been able to show that in silicon grown on a chemically polished silicon substrate the three sides of the trihedra are each single intrinsic faults (Booker and Stickler 1963). The trihedra we observed are too small for the nature of their faults to be determined by x-ray topography.

The defects which appear as triangles on a {111} plane inclined to the crystal face may contain micro-twin lamellae or a number of stacking faults. There could be present twin lamellae many hundred angstroms thick without noticeably modifying the stacking-fault contrast in x-ray topographs. If there is a succession of similar stacking faults all we can conclude is that their number is not divisible by three. Again, all we can

conclude strictly about the dislocation configuration at the bounding edges of the triangles is that the *resultant* Burgers vector is always $\frac{1}{3}\langle 111\rangle$ normal to the plane of the triangle. In the absence of evidence to the contrary we suggest that these single-plane defects comprise a single missing or added layer in the f.c.c. stacking sequence. (This is, of course, a double layer of atoms in the diamond structure (Hornstra 1958).) They may propagate from one edge of an island of a wrongly stacked layer on the horizon H. Our Burgers vector findings coincide with those of Booker and Tunstall (Booker 1964) who find that similar triangles in silicon are bounded by $\frac{1}{3}\langle 111\rangle$ Frank dislocations, sometimes dissociated.

§ 3. The Interior Tetrahedral Defect

The position of the single tetrahedral defect circled in fig. 2 shows that it lies in the $(\bar{1}\bar{1}\bar{1})$ growth sector of the crystal. The orientation of the tetrahedron relative to the growth direction is similar to that of the trihedra in figs. 3 and 4. We interpret the tetrahedron as arising from the termination of a trihedral growth defect by capping with a fault plane on the growth front. This conclusion is supported by the diffraction evidence. No diffraction contrast arises from imperfection within the *volume* of the tetrahedron. This volume appears to be perfect crystal in strictly parallel orientation with the surrounding crystal. *Area* diffraction contrast is obtained from faces of the tetrahedron when the Bragg plane does not coincide with the face or does not lie in the zone of the face-normal. Thus in 111-type reflections three out of four faces produce contrast, and in 220-type reflections two out of four. Figure 6 compares stereopairs of limited projection topograph images of 111 and 220-type reflections with the respective images. The difference between our tetrahedron images and those predicted and observed for 220-type reflections by Pashley and Presland (1961) in electron microscope studies of gold foils arises from the higher Bragg angle and different orientation of the tetrahedron with respect to the incident beam in our case. The density of the image depends upon the ratio of cross-sectional area of primary beam intercepted by the face to that of the diffracted beam leaving it. In the case of the 220-type reflections the expected ratio of densities from the two active faces is $\sin^2(\alpha+\theta_B)/\sin^2(\alpha-\theta_B)\sim 4$ (θ_B is the Bragg angle, α is the angle between Bragg plane and the face). We have confirmed that all faces of the tetrahedron have similar diffraction properties. The large size of the tetrahedron (edge length 115 μm) excludes the possibility of its production from collapse of a triangular vacancy disc in the grown crystal (as can occur on a much smaller scale in quenched metals (Silcox and Hirsch 1959)). We can obtain no direct evidence on the nature of the dislocations along the $\langle 110\rangle$ edges of the tetrahedron. If they are simply the stair-rod type with small Burgers vector $\frac{1}{6}\langle 110\rangle$ we would not expect to see them in the presence of area contrast from the faces.

Interference fringes appear in section topograph images of the tetrahedron. Two sequences of section topographs taken under the geometrical

Fig. 6

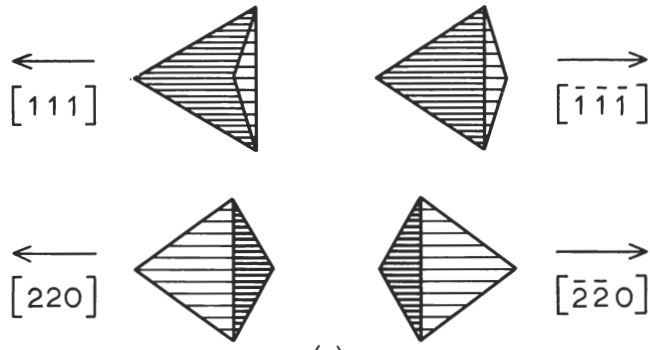

(*a*)

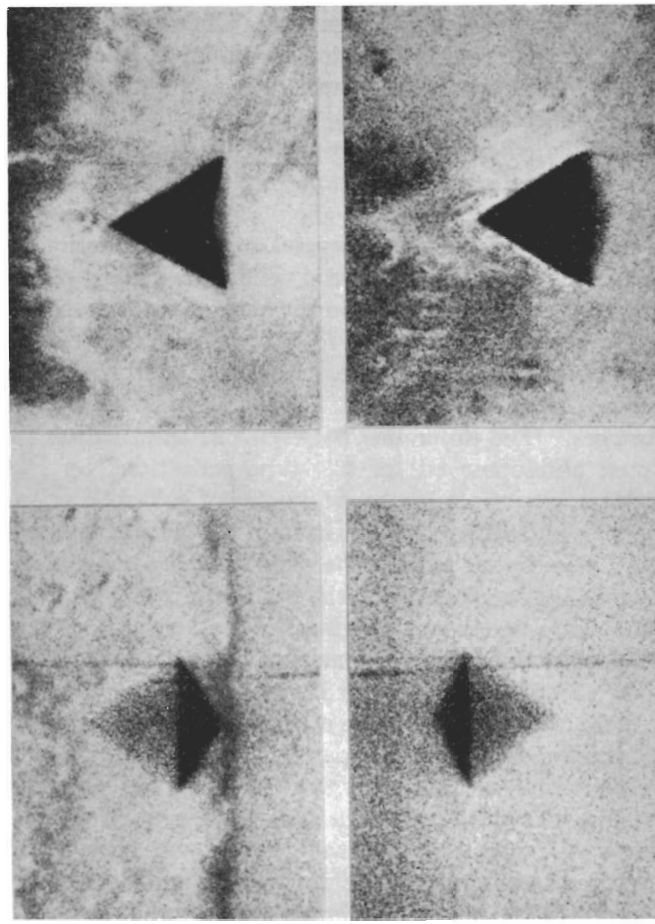

(*b*)

(*a*) Expected projection topograph images of regular tetrahedron in 111 and 220 stereopairs. Shading density proportional to image density. (*b*) observed images.

conditions shown schematically in figs. 7 (*a*) and (*b*) are reproduced in figs. 8 (*a*) and (*b*) respectively. Between each exposure the point of incidence of x-rays on the crystal was translated 50 μm in the direction T: the lines parallel to OA therefore represent successive positions of the incident beam. In the first two sections in figs. 7 (*a*) and 8 (*a*) and in the last two in figs. 7 (*b*) and 8 (*b*) the tetrahedron is cut by the incident beam. In all other sections the image of the tetrahedron is formed by the scattering of x-rays fanning out within the triangle of energy flow, i.e. the triangle AOB in the case of incident beam along OA. No image is formed by parts of the tetrahedron outside the triangle. For clarity in fig. 7 the size of the tetrahedron and the translation steps are exaggerated some twenty-fold with respect to the distance between x-ray entrance and exit surfaces of the crystal. In fact in all section topographs shown here the tetrahedron lies relatively close to the side of the energy-flow triangle parallel to the incident beam.

Fig. 7

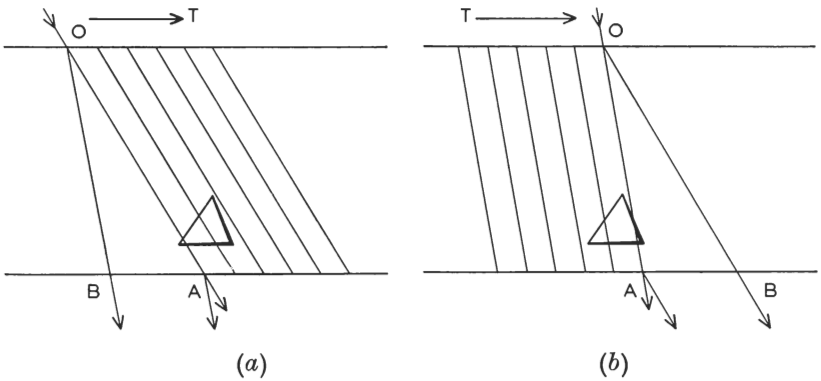

Plan on plane of incidence showing beam positions in series of section topographs taken in sequence indicated by arrow T. When incident beam strikes crystal at O on entrance surface (111) the diffracted beam leaves crystal between A and B on exit surface ($\bar{1}\bar{1}\bar{1}$), Mo Kα radiation, $2\theta_B = 20°$. (*a*) $\bar{1}\bar{1}1$ reflection, (*b*) $11\bar{1}$ reflection.

The tetrahedron images in fig. 8 are rather confused by interference from images of natural damage and nearby saw cuts on the faces, and by some internal strain. Nevertheless, in most cases one can see both the principal image having fringes with intensity maxima greater than average background level, and the weak ghost image with complementary fringes, giving intensity minima less than background level. Since there is no electron microscope counterpart of the separate principal and ghost images we will outline how they are produced in x-ray topographs.

Representative paths of rays producing the principal image P and the ghost image G in the setting of figs. 7 (*a*) and 8 (*a*) are shown schematically in fig. 9 (*a*). The plane of incidence intersects the tetrahedron in the triangle DEF (exaggerated in size). EF and DF are traces of the ($11\bar{1}$) and

Fig. 8

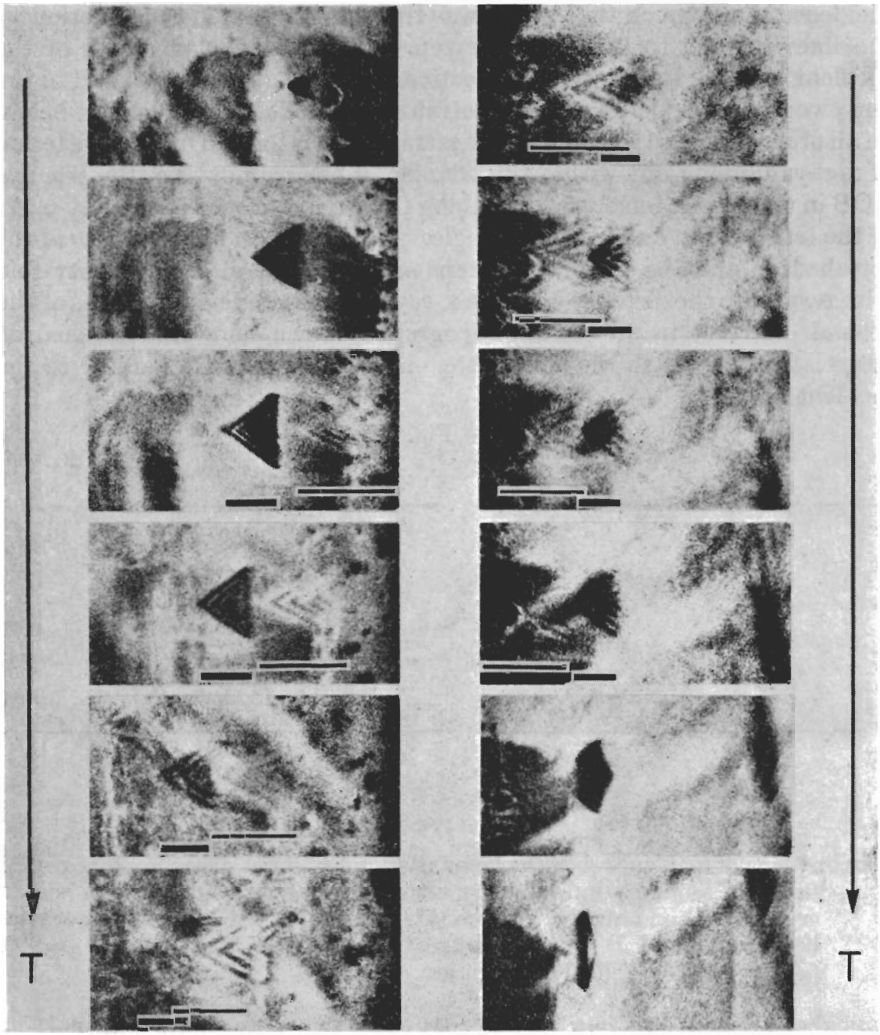

(*a*) (*b*)

Portions of section topographs taken in sequence indicated by arrow T. On each topograph the thick line indicates the calculated position and width of the principal image, and the thin line that of the ghost image. (*a*) $\bar{1}11$ reflections, setting of fig. 7 (*a*), edge A of section coincides with right-hand edge of print, (*b*) $11\bar{1}$ reflections, setting of fig. 7 (*b*), edge A of section coincides with left-hand edge of print. (Damage on surface at A produces strong blackening.)

($\bar{1}\bar{1}\bar{1}$) faces normal to the plane of incidence. DE may represent the trace of either the ($1\bar{1}1$) or ($\bar{1}11$) faces which are inclined to the plane of incidence. A section of the dispersion surface by the plane of incidence in the neighbourhood of the Brillouin plane X parallel to ($11\bar{1}$) appears in fig. 9 (*b*). A ray such as 1 in fig. 9 (*a*) flows along the normal to the dispersion surface at its corresponding wave point 1 in fig. 9 (*b*) (Ewald 1958, Kato 1958). Since the beam incident upon the crystal behaves as a coherent spherical wave (Kato and Lang 1959, Kato 1961) the conjugate wave points 1 and 1′ are both coherently excited in the production of the ray 1. Fault surfaces

Fig. 9

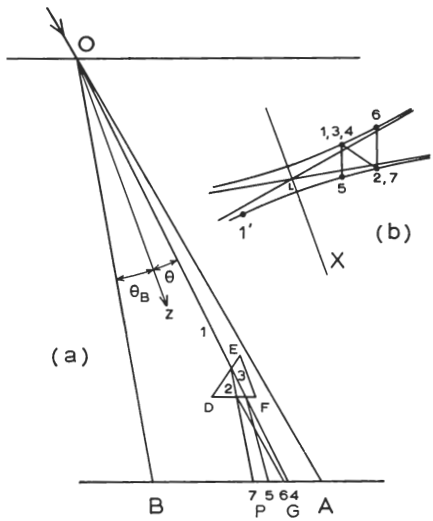

(*a*) Representative ray paths in setting of fig. 7 (*a*). Rays such as 5 and 7 contribute to principal image P. Rays such as 4 and 6 contribute to ghost image G. (*b*) Section of dispersion surface showing wave points 1 to 7 and their connecting tie-lines normal to the fault surfaces.

in the crystal cause new wave points to be excited. However, the pattern of excited wave points on the right of the Brillouin plane X is related to that on the left by inversion through the point L. Consequently the differences between excited wave vectors are numerically equal on either side of X, and both sets of waves interfere similarly in P and G. Hence we need consider only the jumps in wave points starting from the wave point 1. The first jump occurs at the face DE within the tetrahedron. We now have a ray 2 nearly parallel to OB and an undeviated ray 3. In order to satisfy the boundary conditions at the fault surface (Whelan and Hirsch 1957) the line joining points 1 and 2 must lie normal to the fault surface. In practice we need only consider the *projection* of this normal on the plane of the dispersion surface section in fig. 9 (*b*). At the face DF both rays 2 and 3 are split as shown. The tie-lines between wave points 3 and 5, and between 2 and 6, lie normal to DF. Note that the ray 7 is closer than 5 to the direction OB, and that ray 6 is closer than ray 4 to the direction OA. On account

of these small differences in direction, and of the divergence between rays 2 and 3 within the tetrahedron, a given point within the images P or G on the exit surface AB receives rays which have left O in slightly different directions. But since such rays are coherent, as already mentioned, interference on AB can take place. In P we are concerned with interference between rays 1, 3, 5 and 1, 2, 7; and in G between rays 1, 3, 4 and 1, 2, 6. The positions of the P and G images have been computed for all section

Fig. 10

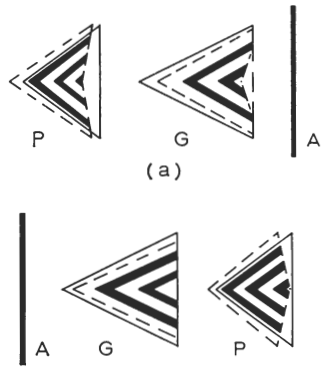

Sketches of expected images. In P, fringes occur in region of overlap of image formed by rays 5 (solid line) and 7 (broken line). In G, fringes occur in region of overlap if image formed by rays 4 (solid line) and 6 (broken line). For clarity, fewer than actual number of fringes are shown. Verticle line represents edge A of section (*a*) $\bar{1}\bar{1}1$ reflection, (*b*) $11\bar{1}$ reflection.

topographs; and in some cases the fringe patterns have been computed as well. Following Kato (1964), the phase difference between rays taking different paths between points in the triangle AOB is calculated by evaluating the difference in the integral $\pm \int \pi D \sqrt{(1-p^2)}\, dz$ for the different trajectories. The coordinate z is measured along the Bragg plane, as shown in fig. 9 (*a*), the sign of the integral depends upon whether the upper or lower branch of the dispersion surface is involved, D is the dispersion surface diameter at the Brillouin plane X and the parameter p is $\tan\theta/\tan\theta_B$. (The angle θ measures the direction of energy flow with respect to the Bragg plane.) Figures 10 (*a*) and (*b*) are sketches of representative images expected in the settings of fig. 7 (*a*) and (*b*), respectively. Agreement between theory and observation is good. When comparing calculated and observed positions of images on fig. 8 it must be borne in mind that the actual width of the ribbon incident beam at the tetrahedron is about 25 μm, half the average translation step, and there is an uncertainty of about 10 μm in each translation setting.

§ 4. Conclusion

The surfaces of this diamond are unusually flat and featureless. No trigons appear at the dislocation outcrops, and the faces exhibit no other

characteristics of etched stones (Lang 1964). Hence the stratifications revealed on the section cut by the $(00\bar{1})$ facet, which repeat at rather regular intervals of about 16 μm extending down to about 200 μm below the surface, should represent the last stages of growth. The nucleation horizons of the outcropping defects do not appear to be associated with any particular phase in the stratification period.

Growth stratifications can usually be traced continuously around diamonds, though individual strata need not maintain the same thickness everywhere. They are interpreted as representing changes of growth conditions with *time* during growth. Breaks in the strata can occur if material has been removed locally during an epoch of solution in the history of the crystal: a good example revealed on etched sections has been described by Harrison and Tolansky (1964). On our specimen we have found no evidence of solution and regrowth and we do not consider that the diffuse triangular patch of imperfection arrowed in fig. 2 is the sole relict of a once continuous sheet surrounding the stone. Rather do we interpret it as due to presence of some impurity on a particular area of the growing crystal surface, growth having occurred under conditions not permitting this impurity to be diffused or carried uniformly over the whole surface.

Acknowledgments

We wish to thank Dr. Eileen Wilks, Clarendon Laboratory, Oxford, for the loan of the diamond, Dr. G. Booker, Cavendish Laboratory, for discussion, and Mr. N. Worth for photographic assistance. We gratefully acknowledge financial support from the Aerospace Research Laboratories, O.A.R., through the European Office of Aerospace Research, United States Air Force. One of us (B.L.) gratefully acknowledges receipt of a British Nylon Spinners Research Fellowship.

References

Booker, G. R., 1964, *Disc. Faraday Soc.*, **38,** 298.
Booker, G. R., and Stickler, R., 1962, *J. appl. Phys.*, **33,** 3281; 1963, *Appl. Phys. Letters*, **3,** 158.
Ewald, P. P., 1958, *Acta Cryst.*, **11,** 888.
Frank, F. C., and Lang, A. R., 1959, *Phil. Mag.*, **4,** 383; 1965, *Physical Properties of Diamonds*, Ed. R. Berman (Oxford: Clarendon Press), Chap. III.
Harrison, E. R., and Tolansky, S., 1964, *Proc. roy. Soc.* A, **279,** 490.
Hornstra, J., 1958, *Phys. Chem. Solids*, **5,** 129.
Kato, N., 1958, *Acta Cryst.*, **11,** 885; 1961, *Ibid.*, **14,** 526, 627; 1964, *J. phys. Soc., Japan*, **19,** 67.
Kato, N., and Lang, A. R., 1959, *Acta Cryst.*, **12,** 787.
Lang, A. R., 1963, *Brit. J. appl. Phys.*, **14,** 904; 1964, *Proc. roy. Soc.* A, **278,** 234.
Pashley, D. W., and Presland, A. E. B., 1961, *Phil. Mag.*, **6,** 1003.
Silcox, J., and Hirsch, P. B., 1959, *Phil. Mag.*, **4,** 72.
Whelan, M. J., and Hirsch, P. B., 1957, *Phil. Mag.*, **3,** 1121.
Wilks, E. M., 1961, *Phil. Mag.*, **6,** 701.
Wilks, E. M., and Wilks, J., 1959, *Phil. Mag.*, **4,** 158.